Microsc. Microanal. 18, 558–567, 2012
doi:10.1017/S143192761200013X

Microscopy AND Microanalysis

Identifying Hexagonal Boron Nitride Monolayers by Transmission Electron Microscopy

Michael L. Odlyzko and K. Andre Mkhoyan*

Department of Chemical Engineering and Materials Science, University of Minnesota, Minneapolis, Minnesota 55455, USA

Abstract: Multislice simulations in the transmission electron microscope (TEM) were used to examine changes in annular-dark-field scanning TEM (ADF-STEM) images, conventional bright-field TEM (BF-CTEM) images, and selected-area electron diffraction (SAED) patterns as atomically thin hexagonal boron nitride (h-BN) samples are tilted up to 500 mrad off of the [0001] zone axis. For monolayer h-BN the contrast of ADF-STEM images and SAED patterns does not change with tilt in this range, while the contrast of BF-CTEM images does change; h-BN multilayer contrast varies strongly with tilt for ADF-STEM imaging, BF-CTEM imaging, and SAED. These results indicate that tilt series analysis in ADF-STEM image mode or SAED mode should permit identification of h-BN monolayers from raw TEM data as well as from quantitative post-processing.

Key words: STEM, ADF, BN, diffraction, tilt, multislice

Introduction

Two-dimensional (2D) materials (Novoselov, 2005), most prominently graphene (Geim & Novoselov, 2007), have recently received heavy attention for their prospective scientific and technological importance. Due to their structure of covalently bonded planes bound by comparatively weak interplanar attractions, layered materials such as graphite and hexagonal boron nitride (h-BN) are among a small handful of materials that can form stable 2D sheet and tube structures, making them important cases for novel condensed matter physics. And because of the exceptional electronic properties and potential for chemical functionalization associated with 2D materials, atomically thin graphite (Geim, 2009; Pumera, 2009) and h-BN (Dean et al., 2010; Golberg et al., 2010) both show promise for use in chemically sensitive devices and next-generation electronics.

Transmission electron microscopy (TEM) is an ideal tool for studying the structure and properties of layered materials, permitting atomic-resolution analysis of material structure by conventional bright-field TEM (BF-CTEM) imaging, scanning TEM (STEM) imaging, or selected-area electron diffraction (SAED), as well as measurements of composition and bonding by electron-energy-loss spectroscopy (EELS). Published studies on graphene have successfully employed SAED (Meyer et al., 2007*a*, 2007*b*), BF-CTEM imaging (Meyer et al., 2008; Girit et al., 2009; Jinschek et al., 2011), annular-dark-field STEM (ADF-STEM) imaging (Gass et al., 2008; Huang et al., 2011), and ADF-STEM imaging with EELS (Suenaga & Koshino, 2010) to characterize the spatial and electronic structure of graphene. Similar studies on h-BN have employed BF-CTEM imaging (Alem et al., 2009; Jin et al., 2009; Meyer et al., 2011) and ADF-STEM imaging (Krivanek et al., 2010; Zan et al., 2011) to characterize the spatial structure of few-layer h-BN.

Meaningful studies of 2D materials require reliable determination of sample thickness, especially in distinguishing single sheets from thicker regions. Thus far, the only explicitly reported means of thickness determination for atomically thin samples of graphite are SAED (Meyer et al., 2007*a*, 2007*b*), through-focal BF-CTEM imaging (Jinschek et al., 2011), relative average ADF-STEM intensities (Gass et al., 2008), and low-loss EELS (Bangert et al., 2008); for graphite samples exhibiting Bernal ABAB stacking, single sheets can presumably also be distinguished by their uniform honeycomb image contrast in an aberration-corrected ADF-STEM. For h-BN, only through-focal BF-CTEM imaging has been explicitly identified as a means of identifying single sheets (Alem et al., 2009; Jin et al., 2009), although variations in column-to-column intensity have also implicitly been used to identify a single sheet in ADF-STEM imaging (Krivanek et al., 2010).

Aside from through-focal BF-CTEM and ADF-STEM line scan analysis, prospective options for h-BN thickness determination in the TEM include low-loss EELS, position-averaged convergent beam electron diffraction (PACBED), and tilt-effect studies. As with graphite (Bangert et al., 2008), thickness-dependent energy shifts of the plasmon peaks may be observable in low-loss EELS, but to the best of our knowledge no theoretical or experimental evidence has yet been presented to suggest this for h-BN and we will not explore the possibility here. PACBED has also been used to discern subtle thickness-dependent changes in zero-disc contrast and thus measure sample thickness to nanometer precision (Loane et al., 1991; LeBeau et al., 2009, 2010; Kourkoutis et al., 2011); we will briefly address the suitability of PACBED for determining the thickness for few-layer h-BN samples. However, we mainly consider the use of

Received August 12, 2011; accepted January 10, 2012
**Corresponding author*. E-mail: mkhoyan@umn.edu

sample tilt to determine the thickness of freestanding atomically thin h-BN.

Methods

ADF-STEM images, BF-CTEM images, and SAED patterns of few-atomic-layer h-BN samples were simulated using the multislice method (Cowley & Moodie, 1957) and code developed by Kirkland (2010). Tilt effects for each characterization mode were simulated using tilted-crystal input files; specimens 1–4 atomic layers thick were studied most intently, at tilts of 0–500 mrad off of the [0001] zone axis at increments of 10 mrad or greater. All simulations were performed at a beam energy of 100 keV, corresponding to conditions for low-damage-rate (Kotakoski et al., 2010) characterization of h-BN.

Supercell sizes of the h-BN specimens used in these simulations were 26.0 × 25.0 Å^2 for ADF-STEM image simulations, 40.96 × 40.96 Å^2 for BF-CTEM image simulations, and 250.0 × 250.0 Å^2 for diffraction simulations; input crystals were simulated using bulk lattice parameters (a = 2.504 Å and c = 6.660 Å) and did not account for the possible surface wrinkling associated with large-area regions (Meyer et al., 2007*a*, 2007*b*) of atomically thin layered materials. For ADF-STEM imaging simulations, optimized slice thicknesses for zone-axis-oriented crystals, crystals tilted 10 to 50 mrad off of [0001], and crystals tilted 100 to 500 mrad off of [0001] were 3.33 Å, 2.00 Å, and 1.50 Å, respectively. For BF-CTEM imaging and diffraction simulations, slice thicknesses were 3.33 Å on the [0001] zone axis and 1.00 Å otherwise. For all tilt effect simulations, the specimen transmission function was calculated with 1,024 × 1,024 pixelation; the probe function for ADF-STEM simulations was also calculated with 1,024 × 1,024 pixelation. For PACBED calculations, both probe and transmission functions were calculated with 4,096 × 4,096 pixelation.

ADF-STEM images were simulated using an aberration-corrected STEM probe with parameters $C_{s(3)} = -0.015$ mm, $C_{s(5)} = 10$ mm, $\Delta f = -30$ Å defocus, and $\alpha_{obj} = 25$ mrad probe-forming objective aperture; although the simulated probe does not explicitly account for the minor effects of chromatic aberration or finite source size, the parameters were chosen to reflect experimentally observed probe characteristics (Mkhoyan et al., 2006, 2008). Electrons scattered 54–340 mrad off of the optic axis were collected to form the ADF-STEM images. Thermal vibrations of the atoms were modeled by averaging 20–40 different frozen phonon configurations (Loane et al., 1991) at temperature 300 K for each ADF-STEM image. Estimated 300 K root-mean-square (RMS) thermal displacements of 0.110 Å and 0.096 Å were used for B and N, respectively, determined by scaling the in-plane RMS displacement of C atoms in graphite (Kelly, 1970) according to the average atomic masses of B and N.

BF-CTEM images were simulated as perfectly coherent images using an aberration-corrected beam with parameters $C_{s(3)} = +0.015$ mm, $C_{s(5)} = 5$ mm, $\Delta f = +91$ Å defocus, and $\alpha_{obj} = 36$ mrad objective aperture cutoff

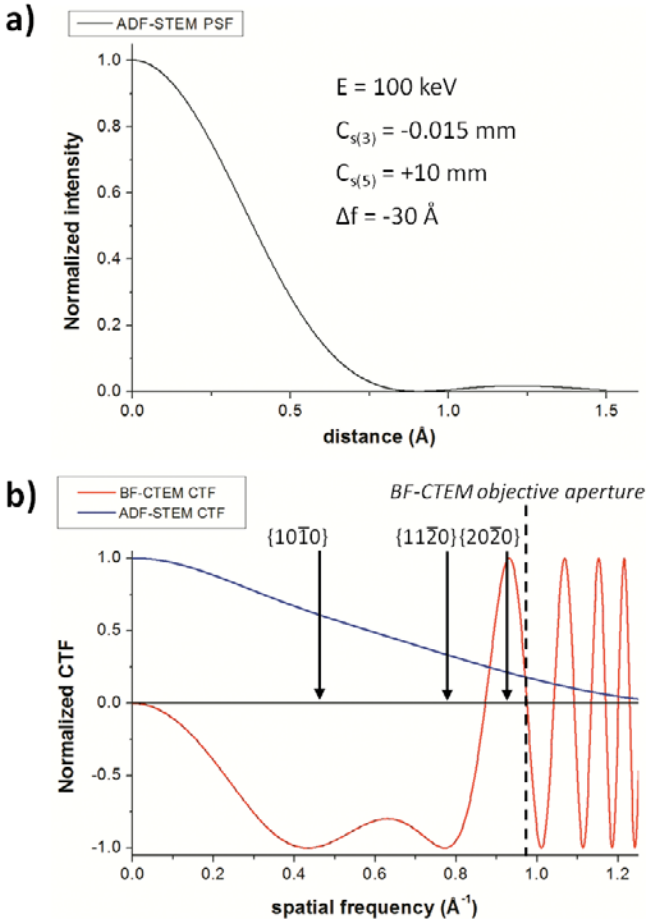

Figure 1. Simulated beam characteristics for 100 keV aberration-corrected TEM imaging of h-BN. **a:** Real-space probe profile for ADF-STEM probe. **b:** Reciprocal-space CTF for ADF-STEM and BF-CTEM probes; spatial frequencies corresponding to Bragg reflections of [0001]-oriented h-BN and to the BF-CTEM objective aperture are overlaid on the plot.

for scattered electrons (Sawada et al., 2005). Effects of chromatic aberration and defocus spread were ignored; thus the simulation output represents an upper bound on the resolution and contrast of an equivalent experimental setup, which typically includes a similar change of sign in the contrast transfer function (CTF) for the highest passed spatial frequencies. Effects of thermal vibrations were modeled by the same means as for ADF-STEM imaging, with 40 frozen phonon configurations being averaged for each image.

The calculated STEM point spread function as well as calculated CTFs for both ADF-STEM and BF-CTEM are presented in Figure 1. While the actual parameters for aberration-corrected and noncorrected imaging vary for different instruments and for different experiments, the general characteristics—such as convergence angles, spherical aberration coefficients, inner and outer angles of the ADF detector, and CTF shapes—are similar, and thus these specific simulated results should be generally applicable.

SAED patterns were simulated with $\beta = 2.0$ mrad convergence semiangle; the slightly convergent beam was

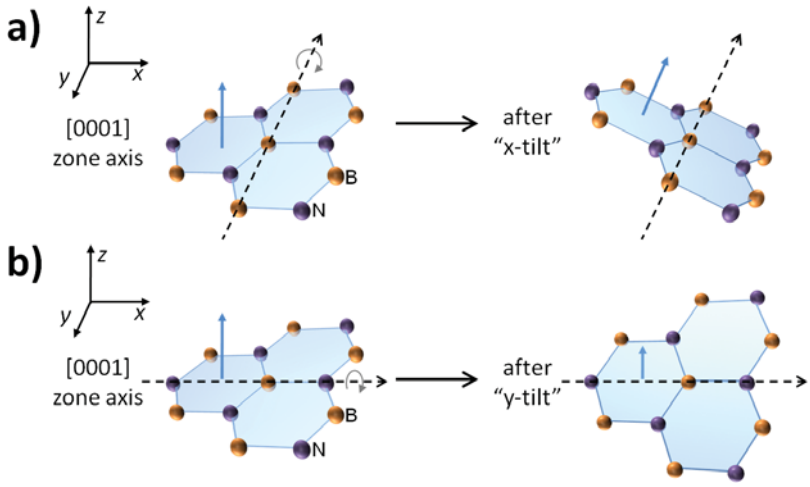

Figure 2. Tilt axis conventions; in each case, the blue vector indicates the [0001] zone axis. **a:** Schematic illustrating an *x*-tilt performed on a single h-BN (0001) plane. **b:** Schematic illustrating a *y*-tilt performed on a single h-BN (0001) plane.

chosen to improve diffraction pattern visibility and prevent artifacts that could arise due to discrete reciprocal-space sampling ($\Delta k = 0.04$ nm^{-1} or $\Delta\alpha = 0.148$ mrad). PACBED patterns were simulated using a strongly underfocused beam with $\beta = 10.6$ mrad convergence semiangle to include an entire "honeycomb" unit within the probe. Effects of thermal vibrations were neglected for SAED because phonons very weakly dampen diffracted spots in the first-order Laue zone, even for 300 K RMS displacements of 0.10 Å for a 100 keV electron beam; they were, however, included for PACBED as 20 frozen phonon configurations at 300 K, so as to avoid overestimating zero-disc contrast (Loane et al., 1991). All simulated SAED patterns are displayed on a linear scale with the central beam saturated to the most intense diffracted-beam pixel of each individual pattern, while CBED patterns are displayed on a linear scale spanning the full range of pattern intensity.

In the following presentation of results and discussion, specimen tilts are referenced to two families of high-symmetry directions in the hexagonal lattice. As illustrated in Figure 2, *x*-tilts are defined as tilts about the *y*-axis (a $\langle 10\bar{1}0\rangle$ direction) while *y*-tilts are defined as tilts about the orthogonal *x*-axis (a $\langle 11\bar{2}0\rangle$ direction). Any arbitrary tilt off of the [0001] zone axis can be constructed as a superposition of tilts in these two directions.

Results

The results of simulations indicate that ADF-STEM images, BF-CTEM images, and SAED patterns from few-layer h-BN are all tilt-sensitive. Each mode of TEM characterization is considered separately below.

Tilt Effects for ADF-STEM Imaging of h-BN

For samples aligned to the [0001] zone axis, there are quantitative differences in column contrast between samples one, two, three, and four layers thick (Fig. 3). Columns with odd numbers of atoms have asymmetric ADF scattering intensities (column-to-column peak intensity differ by 40% and 15% for one and three layers, respectively) while columns with even numbers of atoms have symmetric ADF scattering intensities.

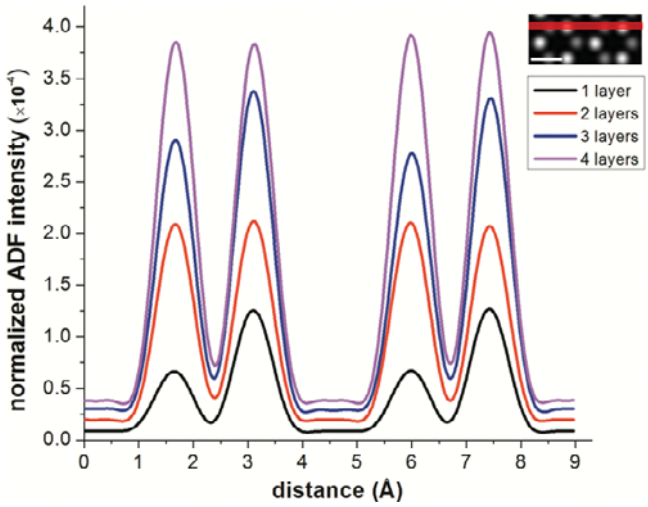

Figure 3. Line scans for [0001]-oriented samples of h-BN along a $\langle 11\bar{2}0\rangle$ direction; the red stripe indicates the six-pixel band of the image for which line scans were performed. ADF detector intensity, normalized to the incident beam current, is plotted on a linear scale.

Tilt effects for ADF-STEM imaging of few-layer h-BN were examined for a 0–500 mrad range for each *x*-tilt (Fig. 4) and *y*-tilt (Fig. 5). For a one-layer-thick sample, tilt only serves to produce a slightly distorted projection of the honeycomb-structured layer; for multiple-layer samples, tilting introduces distinctive complex streaking distortions to the images, with the tilt series for each thickness being clearly distinctive from the others. In all cases, as expected, distortions occur in the direction perpendicular to the tilt axis.

Tilt Effects for BF-CTEM Imaging of h-BN

Tilt effects for BF-CTEM imaging of single and few-layer h-BN were examined for a 0–500 mrad range for each *x*-tilt (Fig. 6) and *y*-tilt (Fig. 7). Tilting introduces complex, intricate distortions to the images for all thicknesses, including the h-BN monolayer.

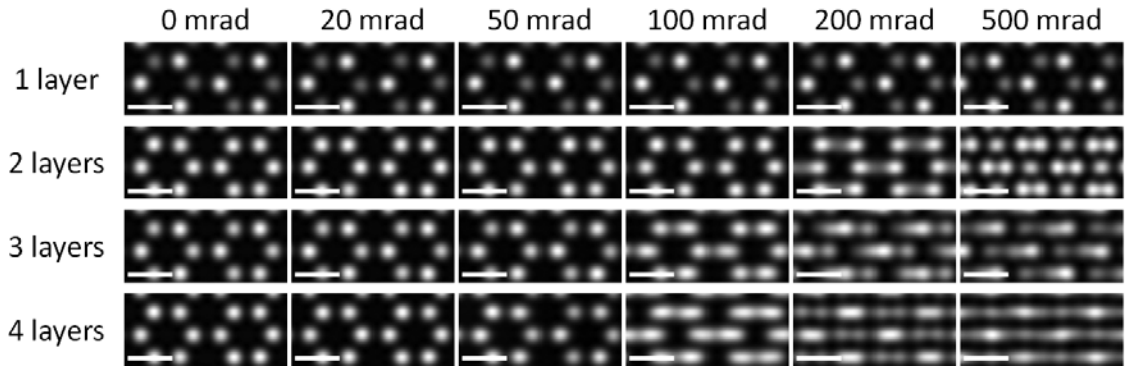

Figure 4. Series of simulated ADF-STEM images of atomically thin h-BN for an aberration-corrected 100 keV TEM, *x*-tilts. For a one-layer-thick region, tilt only serves to produce a distorted projection of the honeycomb-structured layer; for multiple-layer regions, tilting introduces distinctive complex distortions to the images, visible as streaking perpendicular to the *y*-axis. Linear intensity scale; scale bar = 2 Å.

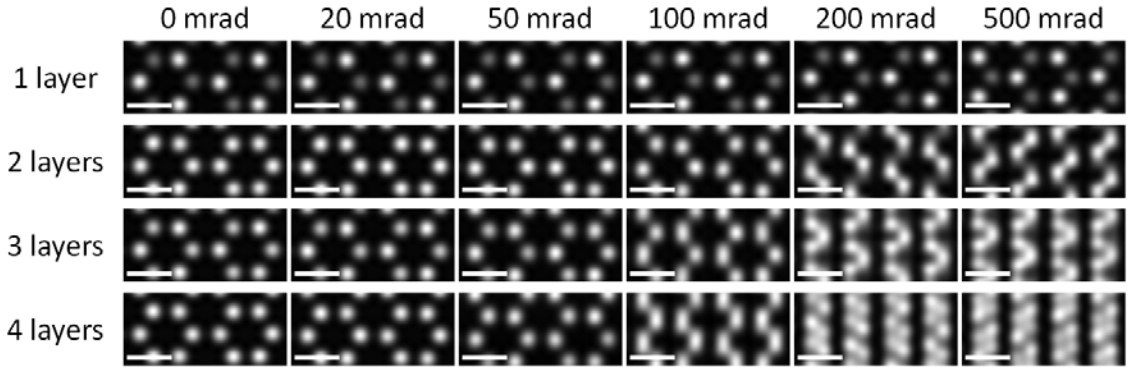

Figure 5. Series of simulated ADF-STEM images of atomically thin h-BN for an aberration-corrected 100 keV TEM, *y*-tilts. For a one-layer-thick region, tilt only serves to produce a distorted projection of the honeycomb-structured layer; for multiple-layer regions, tilting introduces distinctive complex distortions to the images, visible as streaking perpendicular to the *x*-axis. Linear intensity scale; scale bar = 2 Å.

Tilt Effects for Electron Diffraction Characterization of h-BN

For samples aligned to the [0001] zone axis, changes in SAED pattern contrast between samples one, two, three, and four layers thick are practically indiscernible, at least with regard to the relative intensities of $\{10\bar{1}0\}$ and $\{11\bar{2}0\}$ directions. A comparison of line scans through these two peaks in SAED patterns from h-BN samples 1–4 layers thick illustrates this (Fig. 8). PACBED patterns, on the other hand, increase in contrast with increasing thickness (Fig. 9)—the minimum of the central disc is 8.0% below the maximum for 1 layer, 15.1% for 2 layers, 21.6% for 3 layers, and 28.2% for 4 layers—but do not clearly differ in pattern symmetry.

Tilt effects for SAED of few-layer h-BN were examined for a 0–500 mrad range for each *x*-tilt (Fig. 10) and *y*-tilt (Fig. 11). For a one-layer-thick sample, SAED patterns are tilt-independent. However, for a multilayered sample, tilting produces changes in diffracted-spot intensity, with the tilt series for each thickness being distinguishable from the others. In all cases, spots appear and disappear in a band perpendicular to the tilt axis.

To show the effect of sample tilt on different thicknesses of h-BN, the intensity of individual diffracted spots is plotted as a function of sample tilt in Figure 12; one $\{10\bar{1}0\}$ and one $\{11\bar{2}0\}$ spot is chosen for each tilt direction, all spots being chosen on account of their strong tilt-sensitivity for a given tilt series. Also, to confirm that there is no distortion induced by the 2 mrad convergence semiangle used for the simulation results presented in Figures 10, 11, and 12, Figure 13 illustrates that the results are quantitatively equivalent, at least for convergence semiangles ranging 0.25–2.00 mrad. Relative noisiness in diffracted spot intensity for the beam with convergence semiangle 0.25 mrad arises from sampling error inherent to the supercell dimensions used in the simulation.

Discussion

In the cases of ADF-STEM imaging, BF-CTEM imaging, and SAED, a distinction between monolayers and multilayers of freestanding h-BN is expected on account of the fundamental distinction between the scattering pattern from a monolayer and those from multilayers. For a single sheet, the sample serves as a single plane of atomic scatterers without appreciable multiple-scattering interactions, irrespective of tilt angle off of the [0001] zone axis (at least at tilt

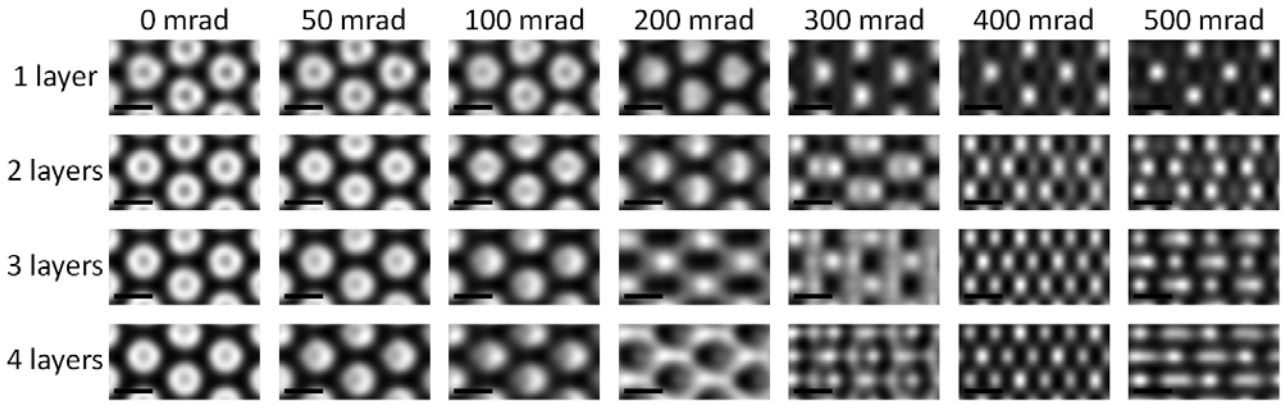

Figure 6. Series of simulated BF-CTEM images of atomically thin h-BN for an aberration-corrected 100 keV TEM, *x*-tilts. For all thicknesses, image contrast evolves in complex fashion as the sample is tilted off of the [0001] zone axis. Linear intensity scale; scale bar = 2 Å.

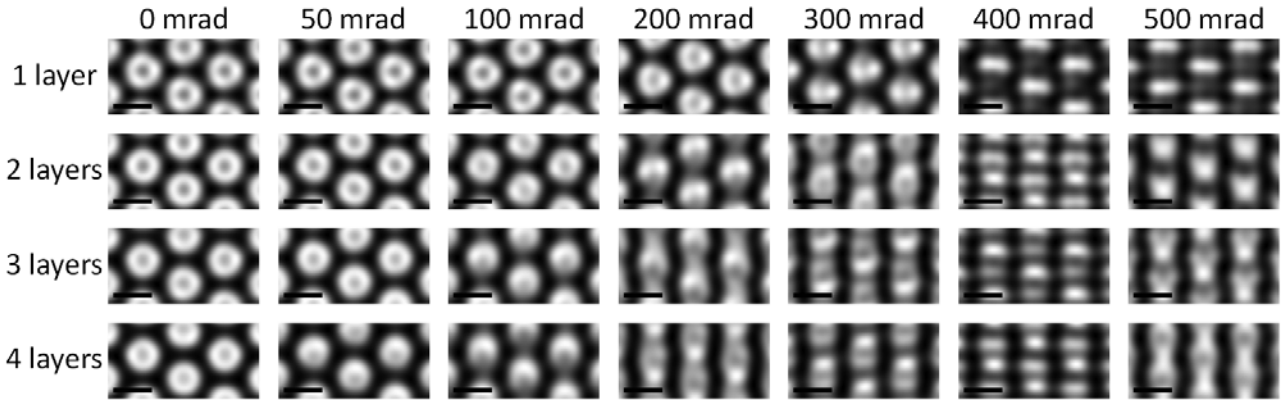

Figure 7. Series of simulated BF-CTEM images of atomically thin h-BN for an aberration-corrected 100 keV TEM, *y*-tilts. For all thicknesses, image contrast evolves in complex fashion as the sample is tilted off of the [0001] zone axis. Linear intensity scale; scale bar = 2 Å.

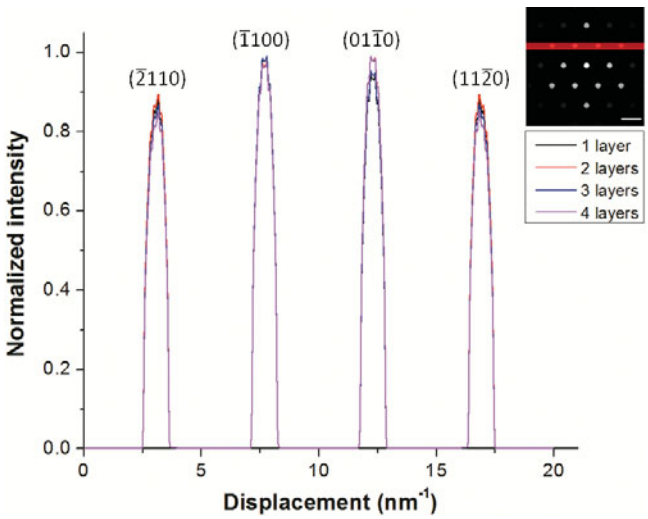

Figure 8. Line scans for [0001]-oriented samples of h-BN through {10$\bar{1}$0} and {11$\bar{2}$0} reflections; red stripe indicates the 29-pixel band of the diffraction pattern for which line scans were performed. Diffracted spot intensities are plotted on a linear intensity scale, with each line scan individually normalized to its maximum value.

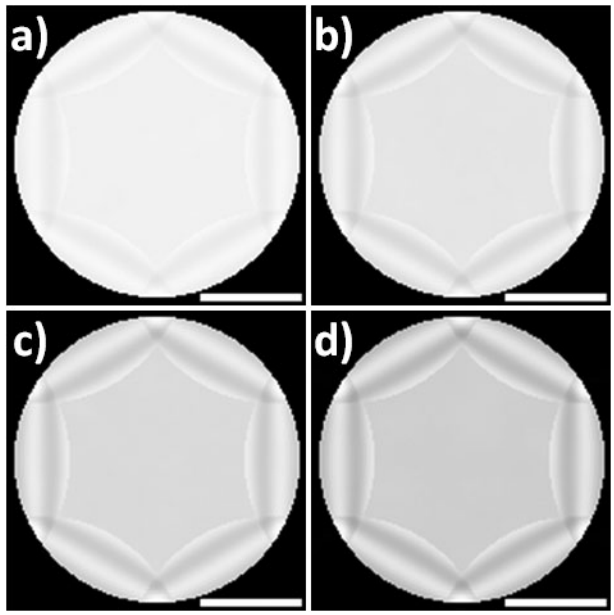

Figure 9. PACBED patterns for [0001]-oriented samples of h-BN (**a**) 1, (**b**) 2, (**c**) 3, and (**d**) 4 atomic layers thick. Linear intensity scale; scale bar = 2 nm^{-1}.

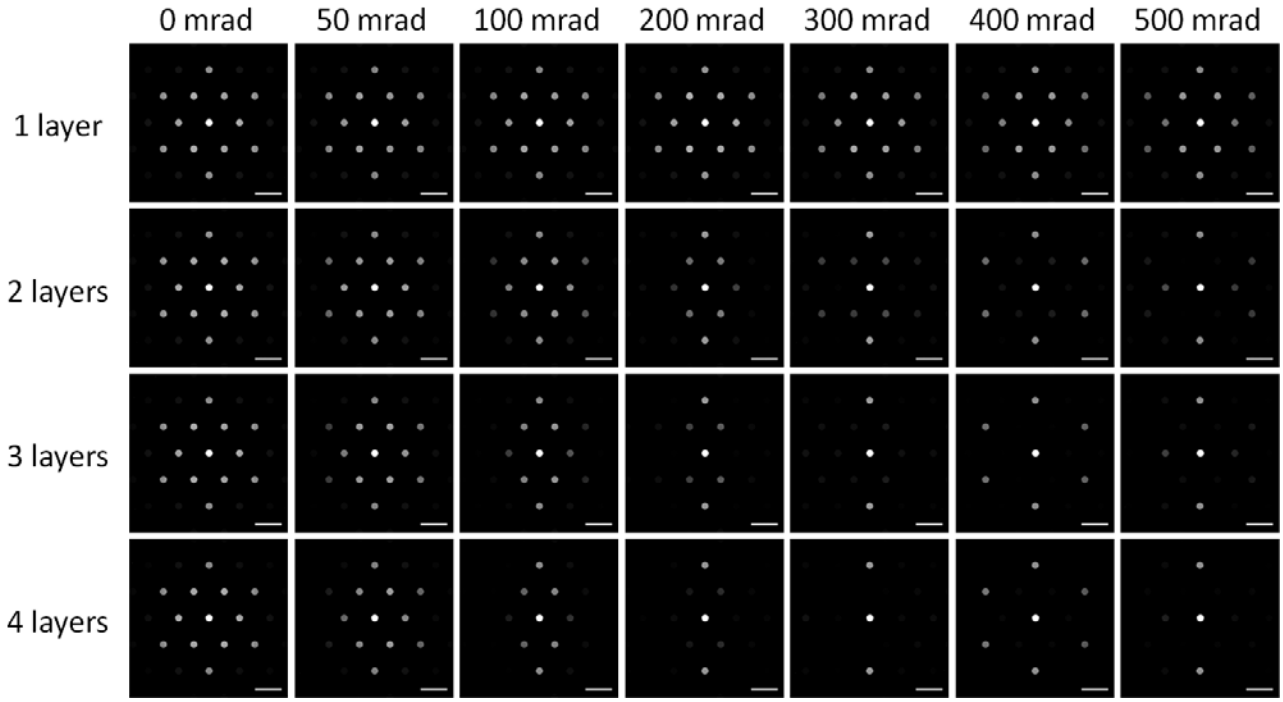

Figure 10. Series of simulated SAED patterns for a 100 keV TEM, *x*-tilts. For a one-layer-thick region, tilt does not change the diffraction pattern contrast; for multiple-layer regions, tilting changes diffracted spot visibility in a band of spots parallel to the *x*-axis. Linear intensity scale; scale bar = 4 nm^{-1}.

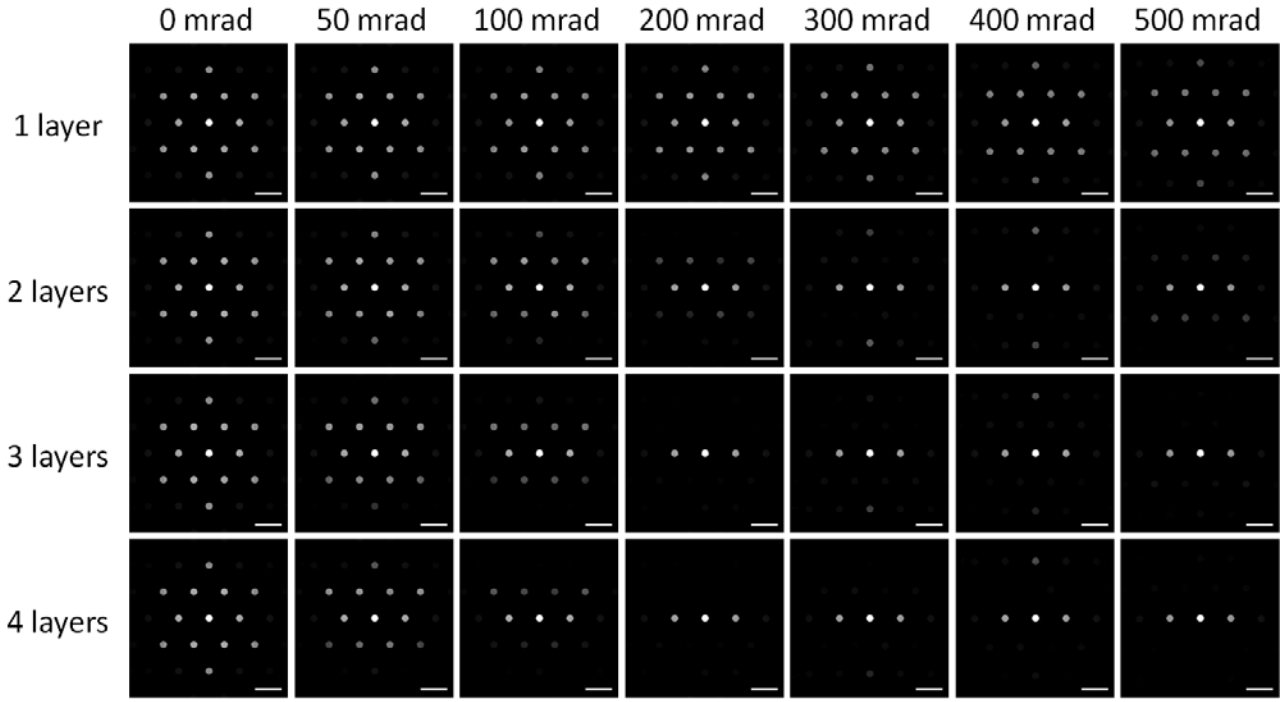

Figure 11. Series of simulated SAED patterns for a 100 keV TEM, *y*-tilts. For a one-layer-thick region, tilt does not change the diffraction pattern contrast; for multiple-layer regions, tilting changes diffracted spot visibility in a band of spots parallel to the *y*-axis. Linear intensity scale; scale bar = 4 nm^{-1}.

angles of up to 500 mrad in *x* or *y*). For samples two atomic layers thick or thicker, the sample serves as a stack of scattering planes where each layer rescatters the electron waves scattered by the layers preceding it in the electron path; when multilayer samples are tilted off of the [0001] zone axis, so that columns of atomic scatterers are no longer parallel to the TEM optic axis, the coherent interference of low-angle-scattering (forming BF-CTEM images and SAED

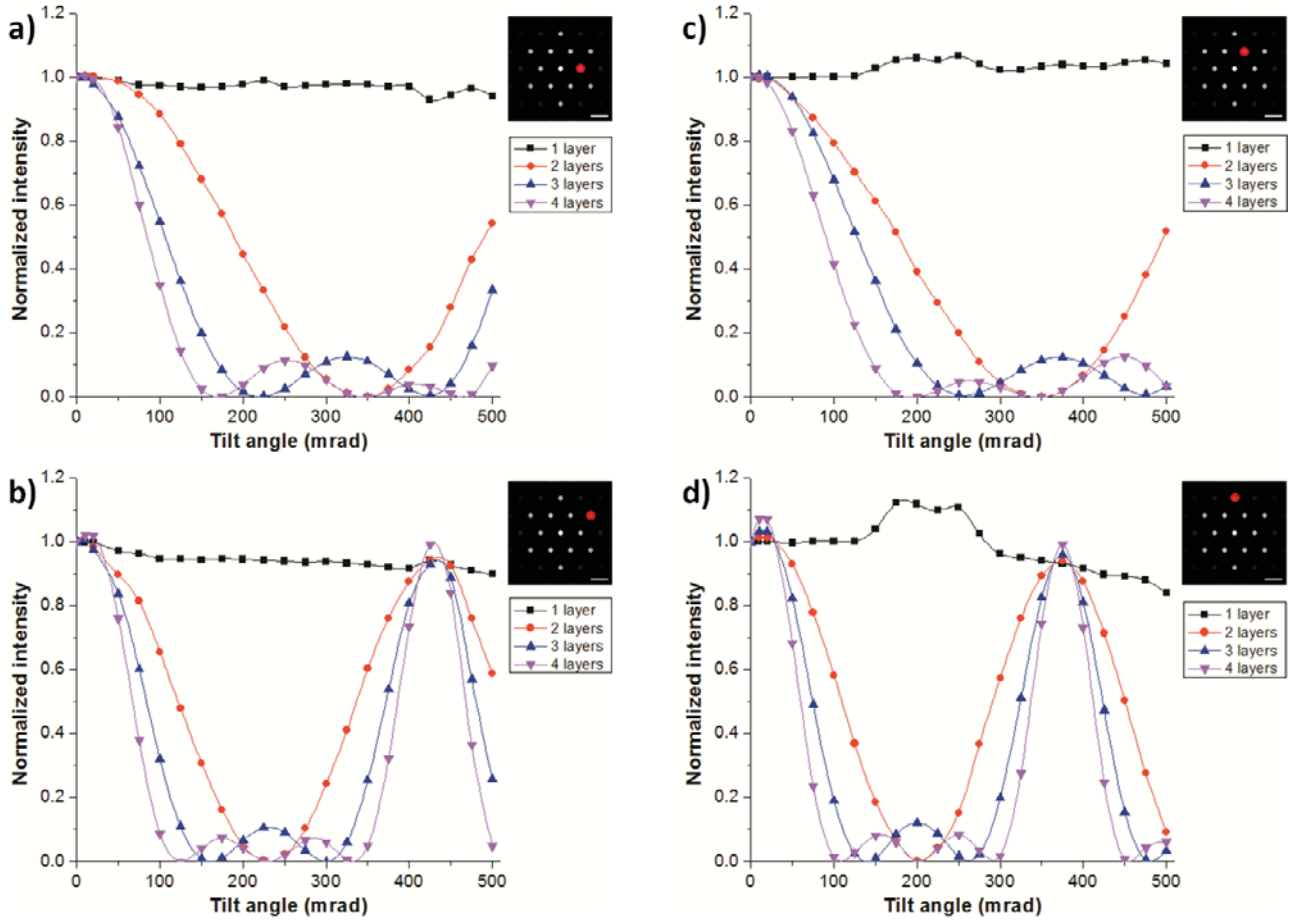

Figure 12. Intensity variation of diffracted spots as a function of tilt angle and sample thickness. For both x-tilt and y-tilt series, one $\{10\bar{1}0\}$ and one $\{11\bar{2}0\}$ reflection was chosen and then analyzed for samples 1–4 layers thick: (**a**) $(10\bar{1}0)$ spot sensitive to x-tilting, (**b**) $(11\bar{2}0)$ spot sensitive to x-tilting, (**c**) $(01\bar{1}0)$ spot sensitive to y-tilting, (**d**) $(\bar{1}2\bar{1}0)$ spot sensitive to y-tilting. Each intensity was calculated as the average of a 7×7-pixel square at the center of the diffracted spot. Each tilt series is normalized to the intensity of the spot at the [0001] zone axis orientation.

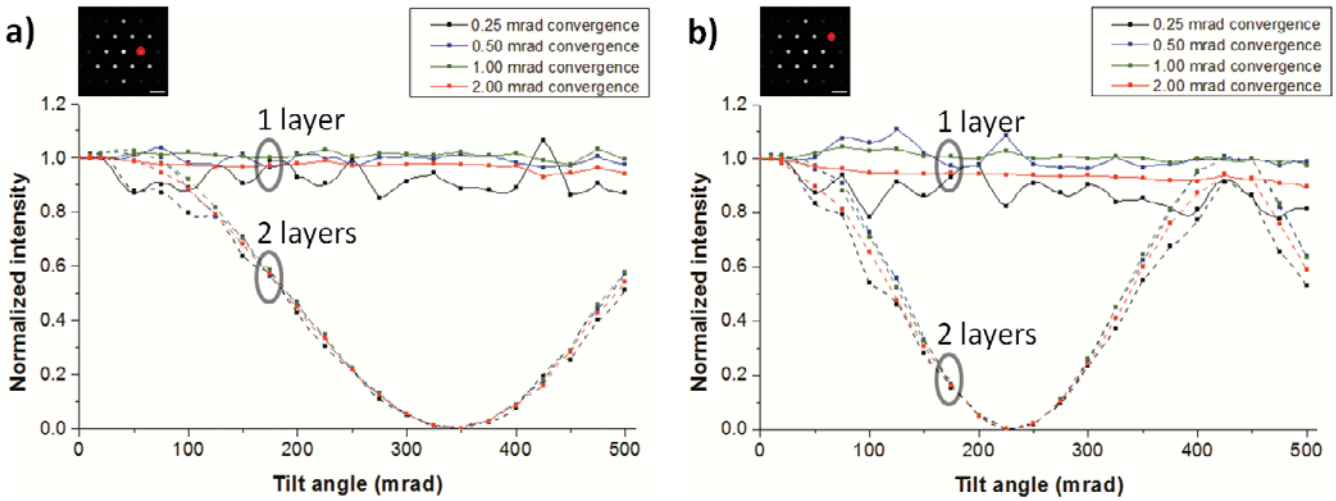

Figure 13. Convergence semiangle dependence for tilt series quantification. **a:** Comparison of $(10\bar{1}0)$ spot intensity for monolayers and bilayers of h-BN. **b:** Comparison of $(11\bar{2}0)$ spot intensity for monolayers and bilayers of h-BN. Intensities were calculated as follows: the average of a 7×7-pixel square for $\beta = 2.00$ mrad, the average of a 5×5-pixel square for $\beta = 1.00$ mrad, the average of a 3×3-pixel square for $\beta = 0.50$ mrad, and the maximum-intensity pixel of the diffracted spot for $\beta = 0.25$ mrad. Relative noisiness in diffracted spot intensity for the beam with convergence semiangle 0.25 mrad arises from sampling error.

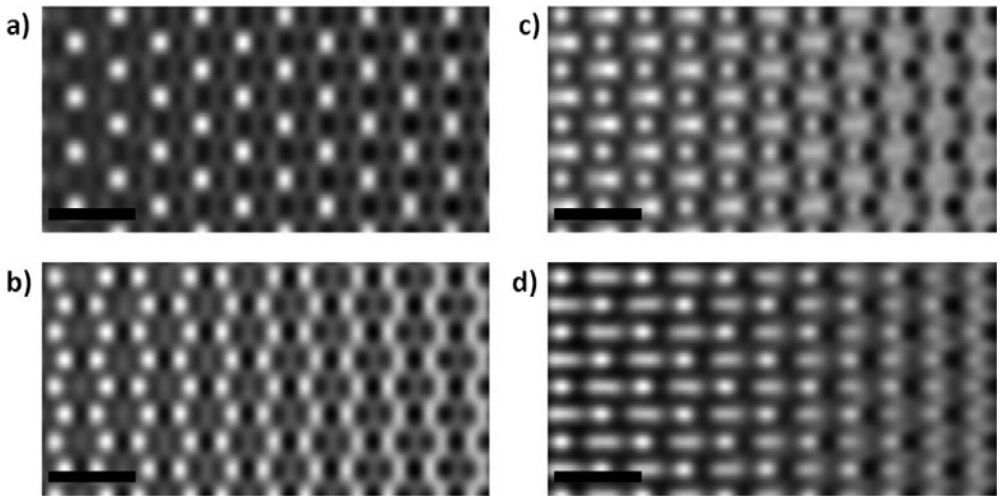

Figure 14. Series of simulated BF-CTEM images for an aberration-corrected 100-keV TEM, with samples tilted to 500 mrad *x*-tilt. (**a**) 1 atomic layer, (**b**) 2 atomic layers, (**c**) 3 atomic layers, and (**d**) 4 atomic layers. Linear intensity scale; scale bar = 4 Å. The variation in position along the optic axis from left to right is 11.2 Å.

patterns) and the lateral distribution of incoherent high-angle-scattering intensity (forming ADF-STEM images) each necessarily deviate from that of a single sheet.

The ADF-STEM simulation data presented above show that, in principle, different thicknesses of h-BN can be distinguished from one another using line scans on raw data and taking the ratio of peak column intensities. Due to the strong *Z*-dependence of high-angle, incoherent elastic scattering (Pennycook & Boatner, 1988; Nellist & Pennycook, 2000), only columns with equal numbers of B and N atoms will have equal intensities. In experiments, however, image noisiness and beam nonidealities may render it impractical to determine the thickness of different regions from relative column intensities, especially from unprocessed data. ADF-STEM imaging over a tilt series, however, permits unambiguous distinction of a single sheet from multilayered samples, and of multilayered samples of different thicknesses, by observing changes in ADF-STEM image contrast over a tilt series. Only a single sheet will not have image contrast change with tilts away from the [0001] zone axis, permitting straightforward identification of freestanding h-BN monolayers. Also, tilting through the 100–500 mrad range would permit distinction between sheets two, three, and four atomic layers thick based on distinctive differences in image contrast between the layers in this tilt range (although possibly only by post-processing of a series of several images acquired at different tilts). Though experimental implementation may be complicated by hysteretic drift of the stage over a tilt series and by the small depth-of-focus of an aberration-corrected STEM instrument, these results should lend themselves to determining sample thickness of few-layer h-BN in aberration-corrected STEM studies (such as the study of defects and edges in atomically thin h-BN).

BF-CTEM results show that distinction between different thicknesses of [0001]-oriented h-BN cannot readily be done using a raw tilt series in these imaging conditions: because all sample thicknesses display pronounced changes in contrast over a tilt series, no single thickness can be readily distinguished using raw image data collected over a tilt series. Even for quantitative through-focal analysis of tilt series data, a major complication for experimental aberration-corrected BF-CTEM imaging of few-layer h-BN would be the high sensitivity of the CTF to defocus (Chang et al., 2003), so that a region of any thickness will have strong variation in contrast as a function of position along the optic axis. When tilted, even a monolayer will vary in contrast across a region of interest (Fig. 14), making it impractical to definitely ascertain its thickness from a BF-CTEM tilt series even by offline processing (let alone qualitative online thickness determination from the raw data).

Employing monochromated illumination together with carefully tuned defocus and an appropriate objective aperture, it is possible to obtain a high-resolution aberration-corrected BF-CTEM image without a sign reversal in the CTF, which in turn could permit identification of monolayer h-BN from a raw tilt series similarly as from a tilt series of ADF-STEM images. However, this is not standard experimental practice (Jinschek et al., 2011; Meyer et al., 2011) and is very difficult to implement given the exacting required conditions and the high sensitivity of CTF structure to defocus; aberration-corrected ADF-STEM is far more robust due to its incoherent imaging mode and associated weakly focus-dependent CTF.

SAED patterns from [0001]-oriented h-BN cannot easily be used to distinguish between different thicknesses of h-BN because, unlike for few-layer graphite (Meyer et al., 2007*a*), there is no significant variation in zone-axis SAED pattern contrast as a function of increasing sample thickness. PACBED patterns from [0001]-oriented h-BN do not show any clear differences in pattern symmetry between samples 1–4 layers thick, so they do not lend themselves to qualitative determination of sample thickness; different thicknesses may be distinguished by the intensity range within the central disc, but even then PACBED could still be

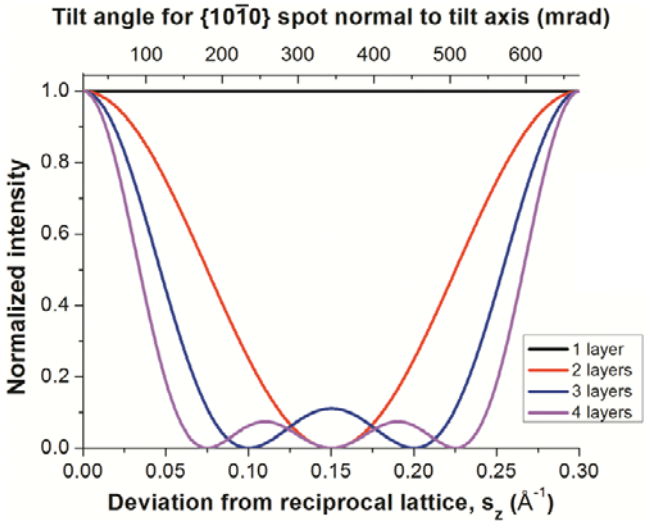

Figure 15. Single-period plot of the relrod intensity for identical atomic layers spaced 3.33 Å apart. If calculated using the scattering factors of B and N atoms with correct stacking order, these intensities would correspond to the exact out-of plane modulation of the relrods (the exact modulation is in fact mapped in the SAED tilt-effect simulations presented previously).

impractical due to presence of experimental noise and the risk of severe beam damage associated with applying the method to few-layer h-BN.

SAED characterization over a tilt series permits unambiguous distinction of a single sheet from multilayered samples, and of multilayered samples of different thicknesses from one another, by observing changes in SAED pattern contrast over a tilt series. Only a single sheet will not have contrast change with tilts away from the [0001] zone axis, whereas diffracted spots strongly vary in intensity over the tilt series for samples two layers and thicker. This effect arises from the three-dimensional (3D) periodicity of the reciprocal lattice—which in turn places a 3D constraint on the Bragg reflection condition—for samples two layers and thicker. By exactly treating the lattice amplitude factor G for a sample of N atomic layers with interlayer spacing c, it can be shown that intensity of the out-of-plane relrod, I, would be a simple function of the deviation from the reciprocal lattice s_z: $I(s_z) = |F_{cell}|^2|G|^2 = I_{\max} \times \sin^2(\pi N c s_z)/\sin^2(\pi c s_z)$. This function is plotted, over one period for a sample with the same interplanar spacing as h-BN, in Figure 15. It is this thickness-dependent relrod structure that accounts for the variations in spot intensity as a function of tilt observed in Figure 12, although the difference in atomic structure between alternating layers of h-BN will modulate the relrods asymmetrically for some of the diffracted spots (e.g., Figs. 12a, 12c).

Also, tilting through the 100–500 mrad range may permit distinction between sheets two, three, and four atomic layers thick based on distinctive differences in SAED contrast between different sample thicknesses (by measuring the angle at which the most tilt-sensitive {10$\bar{1}$0} spot disappears and comparing against the different characteristic angles at which it would disappear for different thicknesses). It is noted, however, that successful experimental implementation of this thickness determination method would require areas of uniform thickness large enough to be exclusively selected by the SAED aperture or by the illumination of a moderately converged beam.

Moderate simplifications employed in these simulations are justified because the first-order Laue zone scattering that determines contrast formation for these SAED patterns is negligibly affected by thermal vibrations with RMS displacements of 0.1 Å, while any possible surface wrinkling present in atomically thin h-BN would only serve to slightly perturb imaging and diffraction from the h-BN lattice. Also, practical application of tilt methods requires careful use of identifying markers to keep track of regions of interest throughout the tilt series, but of course this is a standard discipline for TEM experiments. Thus we anticipate experimental verification of these computational predictions.

Conclusion

Results from multislice simulations indicate that each of ADF-STEM imaging, BF-CTEM imaging, and SAED are tilt-sensitive, but only ADF-STEM imaging and SAED can readily be employed to identify a freestanding h-BN monolayer. Although careful ADF-STEM imaging or PACBED characterization of [0001]-oriented h-BN can potentially be used to measure sample thickness, observing the evolution of an ADF-STEM image or SAED pattern with tilt is a clearer means of identifying h-BN monolayers from raw TEM data. Additionally, these simulation results indicate that ADF-STEM images and SAED patterns collected for a tilt series off of the [0001] zone axis could be used to identify regions two, three, or four atomic layers thick. These results will serve to help future analytical TEM studies of h-BN by providing methods other than BF-CTEM through-focal reconstruction for determining the thickness of few-atomic-layer h-BN.

Acknowledgments

This work was supported partially by the National Science Foundation under award number DMR-1006706 and the University of Minnesota Graduate School Fellowship. We also acknowledge receiving access to computational resources from the University of Minnesota Supercomputing Institute.

References

Alem, N., Erni, R., Kisielowski, C., Rossell, M., Gannett, W. & Zettl, A. (2009). Atomically thin hexagonal boron nitride probed by ultrahigh-resolution transmission electron microscopy. *Phys Rev B* **80**, 155425.

Bangert, U., Eberlein, T., Nair, R.R., Jones, R., Gass, M., Bleloch, A.L., Novoselov, K.S., Geim, A. & Briddon, P.R. (2008). STEM plasmon spectroscopy of free standing graphene. *Phys Stat Sol A* **205**, 2265–2269.

Chang, L.Y., Chen, F.R., Kirkland, A.I. & Kai, J.J. (2003). Calculations of spherical aberration-corrected imaging behaviour. *J Electron Microsc* **52**, 359–364.

Cowley, J. & Moodie, A. (1957). The scattering of electrons by atoms and crystals: A new theoretical approach. *Acta Crystallogr* **10**, 609–619.

Dean, C.R., Young, A.F., Meric, I., Lee, C., Wang, L., Sorgenfrei, S., Watanabe, K., Taniguchi, T., Kim, P., Shepard, K.L. & Hone, J. (2010). Boron nitride substrates for high-quality graphene electronics. *Nat Nanotech* **5**, 722–726.

Gass, M.H., Bangert, U., Bleloch, A.L., Wang, P., Nair, R.R. & Geim, A.K. (2008). Free-standing graphene at atomic resolution. *Nat Nanotech* **3**, 676–681.

Geim, A.K. (2009). Graphene: Status and prospects. *Science* **324**, 1530–1534.

Geim, A.K. & Novoselov, K.S. (2007). The rise of graphene. *Nat Mater* **6**, 183–191.

Girit, C.O., Meyer, J.C., Erni, R., Rossell, M.D., Kisielowski, C., Yang, L., Park, C.-H., Crommie, M.F., Cohen, M.L., Louie, S.G. & Zettl, A. (2009). Graphene at the edge: Stability and dynamics. *Science* **323**, 1705–1708.

Golberg, D., Bando, Y., Huang, Y., Terao, T., Mitome, M., Tang, C. & Zhi, C. (2010). Boron nitride nanotubes and nanosheets. *ACS Nano* **4**, 2979–2993.

Huang, P.Y., Ruiz-Vargas, C.S., van der Zande, A.M., Whitney, W.S., Levendorf, M.P., Kevek, J.W., Garg, S., Alden, J.S., Hustedt, C.J., Zhu, Y., Park, J., McEuen, P.L. & Muller, D.A. (2011). Grains and grain boundaries in single-layer graphene atomic patchwork quilts. *Nature* **469**, 389–392.

Jin, C., Lin, F., Suenaga, K. & Iijima, S. (2009). Fabrication of a freestanding boron nitride single layer and its defect assignments. *Phys Rev Lett* **102**, 195505.

Jinschek, J.R., Yucelen, E., Calderon, H.A. & Freitag, B. (2011). Quantitative atomic 3-d imaging of single/double sheet graphene structure. *Carbon* **49**, 556–562.

Kelly, B. (1970). Thermal vibration amplitudes of carbon atoms in the graphite lattice parallel to the basal planes. *J Nucl Mater* **34**, 189–192.

Kirkland, E.J. (2010). *Advanced Computing in Electron Microscopy*, 2nd ed. New York: Springer.

Kotakoski, J., Jin, C., Lehtinen, O., Suenaga, K. & Krasheninnikov, A. (2010). Electron knock-on damage in hexagonal boron nitride monolayers. *Phys Rev B* **82**, 113404.

Kourkoutis, L.F., Parker, M.K., Vaithyanathan, V., Schlom, D.G. & Muller, D.A. (2011). Direct measurement of electron channeling in a crystal using scanning transmission electron microsopy. *Phys Rev B* **84**, 075485.

Krivanek, O.L., Chisholm, M.F., Nicolosi, V., Pennycook, T.J., Corbin, G.J., Dellby, N., Murfitt, M.F., Own, C.S., Szilagyi, Z.S., Oxley, M.P., Pantelides, S.T. & Pennycook, S.J. (2010). Atom-by-atom structural and chemical analysis by annular dark-field electron microscopy. *Nature* **464**, 571–574.

LeBeau, J.M., Findlay, S.D., Allen, L.J. & Stemmer, S. (2010). Position averaged convergent beam electron diffraction: Theory and applications. *Ultramicroscopy* **110**, 118–125.

LeBeau, J.M., Findlay, S.D., Wang, X., Jacobson, A.J., Allen, L.J. & Stemmer, S. (2009). High-angle scattering of fast electrons from crystals containing heavy elements: Simulation and experiment. *Phys Rev B* **79**, 214110.

Loane, R.F., Xu, P. & Silcox, J. (1991). Thermal vibrations in convergent-beam electron diffraction. *Acta Crystallogr A* **47**, 267–278.

Meyer, J.C., Geim, A.K., Katsnelson, M.I., Novoselov, K.S., Booth, T.J. & Roth, S. (2007*a*). The structure of suspended graphene sheets. *Nature* **446**, 60–63.

Meyer, J., Geim, A., Katsnelson, M., Novoselov, K., Obergfell, D., Roth, S., Girit, C. & Zettl, A. (2007*b*). On the roughness of single- and bi-layer graphene membranes. *Solid State Comm* **143**, 101–109.

Meyer, J.C., Kisielowski, C., Erni, R., Rossell, M.D., Crommie, M.F. & Zettl, A. (2008). Direct imaging of lattice atoms and topological defects in graphene membranes. *Nano Lett* **8**, 3582–3586.

Meyer, J.C., Kurasch, S., Park, H.J., Skakalova, V., Knzel, D., Gro, A., Chuvilin, A., Algara-Siller, G., Roth, S., Iwasaki, T., Starke, U., Smet, J.H. & Kaiser, U. (2011). Experimental analysis of charge redistribution due to chemical bonding by high-resolution transmission electron microscopy. *Nat Mater* **10**, 209–215.

Mkhoyan, K.A., Batson, P.E., Cha, J., Schaff, W.J. & Silcox, J. (2006). Direct determination of local lattice polarity in crystals. *Science* **312**, 1354.

Mkhoyan, K.A., Maccagnano-Zacher, S.E., Kirkland, E.J. & Silcox, J. (2008). Effects of amorphous layers on ADF-STEM imaging. *Ultramicroscopy* **108**, 791–803.

Nellist, P.D. & Pennycook, S.J. (2000). The principles and interpretation of annular dark-field Z-contrast imaging. *Adv Imag Electron Phys* **113**, 147–203.

Novoselov, K.S. (2005). Two-dimensional atomic crystals. *Proc Natl Acad Sci USA* **102**, 10451–10453.

Pennycook, S.J. & Boatner, L.A. (1988). Chemically sensitive structure-imaging with a scanning transmission electron microscope. *Nature* **336**, 565–567.

Pumera, M. (2009). Electrochemistry of graphene: New horizons for sensing and energy storage. *Chem Rec* **9**, 211–223.

Sawada, H., Tomita, T., Naruse, M., Honda, T., Hambridge, P., Hartel, P., Haider, M., Hetherington, C., Doole, R., Kirkland, A., Hutchison, J., Titchmarsh, J. & Cockayne, D. (2005). Experimental evaluation of a spherical aberration-corrected TEM and STEM. *J Electr Microsc* **54**, 119–121.

Suenaga, K. & Koshino, M. (2010). Atom-by-atom spectroscopy at graphene edge. *Nature* **468**, 1088–1090.

Zan, R., Bangert, U., Ramasse, Q. & Novoselov, K. (2011). Imaging of Bernal stacked and misoriented graphene and boron nitride: Experiment and simulation. *J Microsc* **244**(2), 152–158.